


Article

Experimental Validation for Mechanically Tunable Defect Bands of a Reconfigurable Phononic Crystal with Permanent Magnets

Jeonggyu Yang and Soo-Ho Jo * 

Department of Mechanical, Robotics, and Energy Engineering, Dongguk University, Seoul 04620, Republic of Korea; yangjg_21258@dgu.ac.kr

* Correspondence: soohojo@dgu.ac.kr; Tel.: +82-2-2260-3702

Abstract: Phononic crystals (PnCs) have garnered significant attention due to their unique ability to control elastic waves in unconventional ways. One area of research focuses on utilizing defects within PnCs. Defects create new pass bands within band gaps, leading to concentrated wave energy within the defects. However, defect-mode-enabled wave localization is effective only at specific frequencies, limiting its usefulness when the frequencies of incident waves vary. Existing methods to mechanically tune defect bands involve changing the geometries of unit cells or defects or attaching elastic foundations, which necessitates the detachment and reattachment of certain structures depending on the engineering situation. Considering these challenges, this study introduces a novel approach that utilizes the reconfigurable PnC design, incorporating permanent magnets and ferromagnetic materials. The case study involves a one-dimensional PnC consisting of a long metal beam with rectangular block-shaped permanent magnets periodically arranged and attached to the beam by magnetic forces. A defect is created by shifting a subset of these block-shaped permanent magnets in parallel. The extent of this parallel movement alters the vibrating characteristics of the defect, facilitating the mechanical control of the defect bands in the defective PnC. The effectiveness of this approach is experimentally validated.

Keywords: phononic crystal; defect; wave localization; permanent magnets; tunable



Citation: Yang, J.; Jo, S.-H. Experimental Validation for Mechanically Tunable Defect Bands of a Reconfigurable Phononic Crystal with Permanent Magnets. *Crystals* **2024**, *14*, 701. <https://doi.org/10.3390/cryst14080701>

Academic Editor: Luis M. Garcia-Raffi

Received: 6 July 2024

Revised: 16 July 2024

Accepted: 29 July 2024

Published: 1 August 2024



Copyright: © 2024 by the authors. Licensee MDPI, Basel, Switzerland. This article is an open access article distributed under the terms and conditions of the Creative Commons Attribution (CC BY) license (<https://creativecommons.org/licenses/by/4.0/>).

1. Introduction

Interest in phononic crystal (PnC) structures is rapidly increasing [1,2]. PnCs are characterized by their periodic arrays of engineered unit cells, which uniquely control elastic waves in unconventional ways. A significant area of research focuses on exploiting imperfections, known as defects, within PnCs to achieve spatial localization of elastic waves and enhance mechanical energy density [3]. In the absence of defects, PnCs exhibit phononic band gaps due to Bragg scattering [4,5]. However, the introduction of defects creates new pass bands, termed defect bands, within the phononic band gaps [6,7]. This phenomenon, known as the defect-mode shape, facilitates a substantial concentration of elastic wave energy in the vicinity of the defect [8,9]. The remarkable wave localization within a narrow frequency range has inspired the development of various applications for defective PnCs, including narrowband pass filters [10], piezoelectric energy harvesters [11], ultrasonic sensors [12], and actuators [13]. Here and hereafter, a PnC containing a defect is referred to as a ‘defective PnC’.

Research on defective PnCs has been approached from multiple perspectives. Advances in modeling have led to the development of analytical models for the rapid computation of defect bands and wave localization performances in one-dimensional structures [14]. Furthermore, numerical models, such as the finite element method, have been constructed to predict similar outcomes in two-dimensional structures [15]. Leveraging these modeling techniques, several innovative designs have been heuristically devised to improve wave localization performance [16–18]. Additionally, structural optimization techniques

have been integrated into the design process. These techniques aim to produce optimal designs that maximize or minimize specific objective functions while satisfying design constraints [19–21]. Recently, with the rapid advancement of hardware and the availability of open-source codes, artificial intelligence has begun to be incorporated into this field. This incorporation allows for the automatic generation of various defective PnC designs tailored to distinct design optimization problems, significantly reducing the need for human intervention [22].

However, there are notable drawbacks associated with defect modes in PnCs. Wave localization is effective only at specific frequencies. If incident waves enter defective PnCs at a frequency slightly different from the designated defect band, the defective PnCs will merely exhibit band-gap performance, resulting in no energy confinement [23–25]. This nullifies the effectiveness of defective PnCs. For instance, consider an engineer utilizing defective PnCs positioned on rotating machinery for piezoelectric energy harvesting to power wireless sensors [26,27] or for bandpass filters in structural health monitoring [28,29]. As the rotational speed of machinery, such as gears [30], motors [31], and bearings [32] varies, the frequency spectrum of the resulting vibrations and waves naturally shifts. If a defective PnC is optimized for only an initial frequency, it becomes highly susceptible to these fluctuating operating conditions. This limitation presents a significant challenge in industrial applications where the excitation frequency is not fixed.

Therefore, it is imperative to devise a design methodology that enables the adjustment of defect bands. Research in this area can be categorized into three main approaches. The first approach involves incorporating temperature-dependent materials in the design phase of defective PnCs [33–35]. These materials exhibit properties that change significantly with variations in the external temperature. However, intentionally controlling the external temperature is challenging, and even with the use of heat patches, there is a notable disadvantage due to their inherently slow response to temperature changes.

To address this issue, the second approach leverages intelligent materials that are additionally attached to defects. For instance, previous studies have explored the use of piezoelectric materials with inductors [36] and synthetic negative capacitors [37]. Inductors create electrical resonance, generating new defect bands and enabling their frequencies to be electrically controlled over the entire band-gap region by adjusting the inductance values. Alternatively, synthetic negative capacitors can significantly manipulate pre-existing defect bands under short-circuit conditions by widely adjusting the equivalent elastic constant of the piezoelectric materials. In addition to piezoelectric materials, dielectric elastomers [38] and magnetostrictive materials [39] are also utilized.

The aforementioned methods involve adjusting defect bands by altering the external environment through changes in temperature, electric field, electric circuit, magnetic field, and similar factors. While these methods are straightforward, they necessitate additional equipment and devices to modify the external environment, which inevitably introduces complexities and inconveniences in the installation and operation of defective PnCs. An alternative, as well as last, approach involves mechanically controlling defect bands.

In previously reported cases, one method involves altering the material or geometry of the unit cell or defect. Li et al. discovered that defect bands changed for a variety of materials, including rubber, steel, lead, copper, aluminum, epoxy, and PMMA [40]. However, since material properties are discrete values, selecting materials based on specific frequencies is impractical. To address this issue, Ma et al. aimed to control defect-band frequencies by modifying the geometric dimensions of defects [41]. Similarly, Jiang et al. adopted a multi-stub design, where the defect itself comprised four structures, and adjusted the defect-band frequencies by altering the arrangement of these structures [42]. Given that geometric dimensions are continuous values, defect bands can be tuned to specific frequencies in a continuous manner. More recently, an elastic foundation has been placed on the exterior of defective PnCs in order not to affect the original PnC design [43]. By adjusting the stiffness of this elastic foundation, the defect-band frequencies can vary along within the band gap. However, these geometry-manipulating design approaches

share a common limitation in controlling elastic waves and vibrations: they are not easily reconfigurable. This necessitates the detachment and reattachment of certain structures depending on the engineering situation. For example, this process may involve melting metal for removal, welding metal for attachment, or utilizing tools such as hammers, nails, and screws. Consequently, this can make the operation of defective PnCs cumbersome.

Inspired by the challenges highlighted in previous research, we propose an intuitive approach to mechanically tune defect bands using only the originally designed defective PnCs and eliminating the need for detaching and reattaching structural components. The proposed reconfigurable defective PnCs are constructed from permanent magnets and ferromagnetic materials. The base beam is composed of ferromagnetic materials, with block-shaped permanent magnets arranged periodically and bonded magnetically through the attraction between the two materials. By altering the relative positioning of designated permanent magnets, we can control the formation and adjustment of defect bands. To validate the effectiveness of this design concept, we conduct a series of experiments. The results demonstrate that our approach allows for the mechanical adjustment of defect bands, thereby confirming the practical applicability of our reconfigurable design. This reconfigurable design reduces operational complexity and provides a more efficient solution for applications requiring simplified dynamic tuning of defect bands. Additionally, easy replacements can be promptly prepared in the event of structural issues, such as fractures in the beam or magnets, thereby restoring the original functionality of the defective PnCs.

The remainder of this paper is organized as follows: Section 2 presents the configuration and specification of the proposed design. Section 3 delineates the numerical results in terms of defect-band frequencies and defect-mode shapes. Section 4 delineates the experimental setup and procedure. Section 5 presents the experimental results and offers an in-depth discussion of mechanically tunable defect bands. Finally, Section 6 provides a summary of the findings and conclusions drawn from this study.

2. Proposed Design

Recall that this proposed design concept is intended to address the limitations of current tuning methods for mechanically tuning defect bands in PnCs. The existing methods require complex geometric alterations or the attachment of elastic foundations, making the adjustment process quite cumbersome. Our novel design leverages reconfigurable PnCs with permanent magnets and ferromagnetic materials, simplifying the tuning process and enhancing the usability of wave-localization phenomena.

Figure 1 illustrates each configuration modeled in COMSOL Multiphysics for the unit cell and the one-dimensional defective PnC that are used in the experiment. In Figure 1a, a rectangular block-shaped permanent magnet (colored in dark blue) is magnetically attached to a metal beam (colored in gray). The metal beam is made of steel, while the permanent magnet block is composed of ferrite. According to the COMSOL Multiphysics data sheet, the steel has a mass density of 7850 kg/m^3 , a Young's modulus of 200 GPa, and a Poisson's ratio of 0.3. For the ferrite magnets, these properties are specified as 5000 kg/m^3 , 200 GPa, and 0.33, respectively, based on data provided by domestic suppliers in the Republic of Korea. The steel beam dimensions are 40 mm in length, 25 mm in width, and 1 mm in thickness. It implies that a lattice constant is 40 mm. The ferrite magnet block is 10 mm in length, 40 mm in width, and 25 mm in thickness, positioned such that the geometric center of its lower surface aligns with the geometric center of the upper surface of the steel beam.

Figure 1b depicts a defective PnC comprising five ferrite magnet blocks. In the case of the defect-free PnC, the periodically arranged ferrite magnet blocks are spaced 40 mm apart. These blocks are securely attached to the top of a long steel beam measuring 300 mm in length. The periodicity is locally disrupted by moving the second through fifth blocks in parallel, altering the length of the steel beam between the first and second blocks, thus creating a defect. The defect length depends on the degree to which the four blocks are moved in parallel, changing the vibrating characteristics of the defect. To avoid confusion,

it should be noted that the defect length refers to the distance between the centers of the first and second ferrite magnet blocks when the defect occurs.

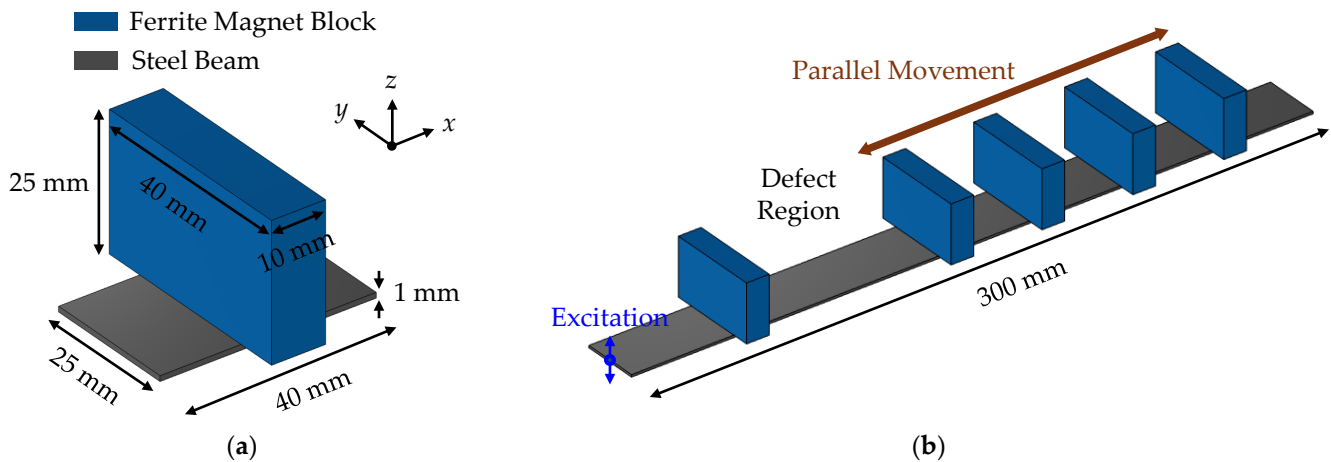


Figure 1. A schematic view of the proposed design concept of defective PnCs: (a) a unit-cell configuration consisting of a steel beam and a ferrite magnet block and (b) a defective PnC configuration consisting of five ferrite magnet blocks attached to the long steel beam.

Adjusting the defect bands of these defective PnCs is both intuitive and straightforward. The magnet positions can be tailored to increase or decrease the defect length. This approach is worth comparing to previously reported designs, where the geometries of defects were changed by substituting several prefabricated prototypes. For elastic waves composed of solid materials, this process involves significant hassle due to repeated assembly and disassembly. In contrast, the current method employs magnetic attachment, allowing for easy adjustment of the mechanical position, similar to magnets on a refrigerator surface. Various types of defects can be designed in real-time and even eliminated without requiring any additional attachments.

At this juncture, two questions may arise at this point: (i) why are ferrite magnets used instead of neodymium magnets, which are the most widely used; and (ii) why is the lattice constant set to 40 mm? The primary objective of this research is to attach a set of permanent magnets to a steel beam and alter their positions. Thus, any magnet with sufficient magnetic force to adhere to the steel beam is adequate. Neodymium magnets exhibit excessively strong magnetic forces, unfortunately resulting in significant interactions between neighboring neodymium magnets. To minimize these interactions, ferrite magnets are selected due to their comparatively weaker magnetic force and cost-effectiveness. In a similar manner, the lattice constant is set to 40 mm because this distance is the minimum at which the magnetic force between adjacent ferrite magnets becomes negligible. Additionally, since each magnet has north and south poles, it is important to arrange the magnets so that one magnet experiences both attractive (or repulsive) forces from two neighboring magnets and finally falls in linear momentum balance. Although this arrangement is not strictly necessary due to the inherent magnetic force between the steel beam and the ferrite magnets, it helps to reduce unwanted disturbances in the experiment. In summary, the selection of the magnet type and the lattice constant is determined by the magnetic flux density (unit: Gauss) of the commercial permanent magnets.

3. Numerical Analysis and Result

Before presenting the experimental results, a preliminary investigation of the numerical analysis and results is conducted. A commercially available finite element analysis tool,

COMSOL Multiphysics 6.1, is employed for all the simulations. The governing equation for elastic wave propagation in solids is as follows:

$$\rho \frac{\partial^2 \mathbf{u}}{\partial t^2} = (\lambda + 2\mu) \nabla \nabla \times \mathbf{u} - \mu \nabla \times \nabla \times \mathbf{u} \quad (1)$$

where ρ represents the mass density, λ and μ are the first and second Lamé constants of the solids, respectively. The vector \mathbf{u} denotes the particle displacement fields; t is the time. To determine the band structures of the unit cell or the defective PnC, the following Floquet–Bloch theorem is taken into account [44]:

$$\mathbf{u}(\mathbf{r} + \bar{\mathbf{r}}) = \mathbf{u}(\mathbf{r}) \exp(i\mathbf{k} \cdot \bar{\mathbf{r}}) \quad (2)$$

where \mathbf{r} is a spatial vector, expressed as $x_1\mathbf{e}_1 + x_2\mathbf{e}_2 + x_3\mathbf{e}_3$, and $\bar{\mathbf{r}}$ is a lattice vector. A reciprocal wave vector \mathbf{k} is included in the first irreducible Brillouin zone, ranging from 0 to π/a , where a represents the spatial length of the unit cell or defective PnC. Under the assumption of time-harmonic motions, an eigenvalue problem can be stipulated by inserting Equation (2) into Equation (1) as:

$$([\mathbf{K}(\mathbf{k})] - \omega^2[\mathbf{M}])\{\mathbf{q}\} = \mathbf{0} \quad (3)$$

where $[\mathbf{K}(\mathbf{k})]$, $[\mathbf{M}]$, and $\{\mathbf{q}\}$ represent the stiffness matrix (as a function of the reciprocal wave vector \mathbf{k}), the mass matrix, and the displacement vector of the targeted structure, respectively. Band structures can be determined by numerically calculating the eigenfrequencies for the given reciprocal wave vector \mathbf{k} within the first irreducible Brillouin zone.

In COMSOL, the physics of solid mechanics and the study of eigenfrequency are activated. The process begins by defining a three-dimensional spatial domain and constructing the unit cell or defective PnC using the block function in the geometry part. The interfaces of different materials automatically incorporate the continuity conditions of displacements and forces. Simultaneously, all surfaces of each structure are configured for traction-free conditions. The Floquet periodicity setting is then applied to both ends of the structures. After testing for convergence, the maximum mesh size is set to 2 mm, utilizing a free tetrahedral mesh type.

First, the phononic band-gap range needs to be identified. Figure 2 displays the numerical results for band structures at the unit-cell level, presenting three different graphs to illustrate the concept of the polarization factor. The polarization factor determines which mode (longitudinal, flexural, and torsional waves) is dominant at a given frequency. This factor is mathematically expressed as follows [45,46]:

$$\text{Polarization Factor} = \frac{\int_V u_i u_i^* dV}{\int_V u_1 u_1^* + u_2 u_2^* + u_3 u_3^* dV} \quad (i \in \{1, 2, 3\}) \quad (4)$$

where V represents the total volumetric domain of the unit cell. u_1 , u_2 , and u_3 denote the displacements in the x -, y -, and z -axes, respectively. The conjugate of a physical quantity p is denoted as p^* . In this study, the flexural waves are targeted, which are predominantly polarized in the z -axis. The closer the polarization factor is to 1 (indicated by red), the more dominant the mode in that direction. Even though all wave types are coupled due to the asymmetrical geometric configuration of the present unit cell [47,48], a comparison of the three graphs reveals that the phononic band gap corresponding to flexural waves spans approximately from 0.78 Hz to (at least) 15 kHz. Note that the graph on the right in Figure 2a shows three flat pass bands, which represent the resonance frequencies of 5.80, 7.23, and 13.85 kHz at the unit-cell level. The resonant mode shapes for these frequencies are depicted in Figure 2b.

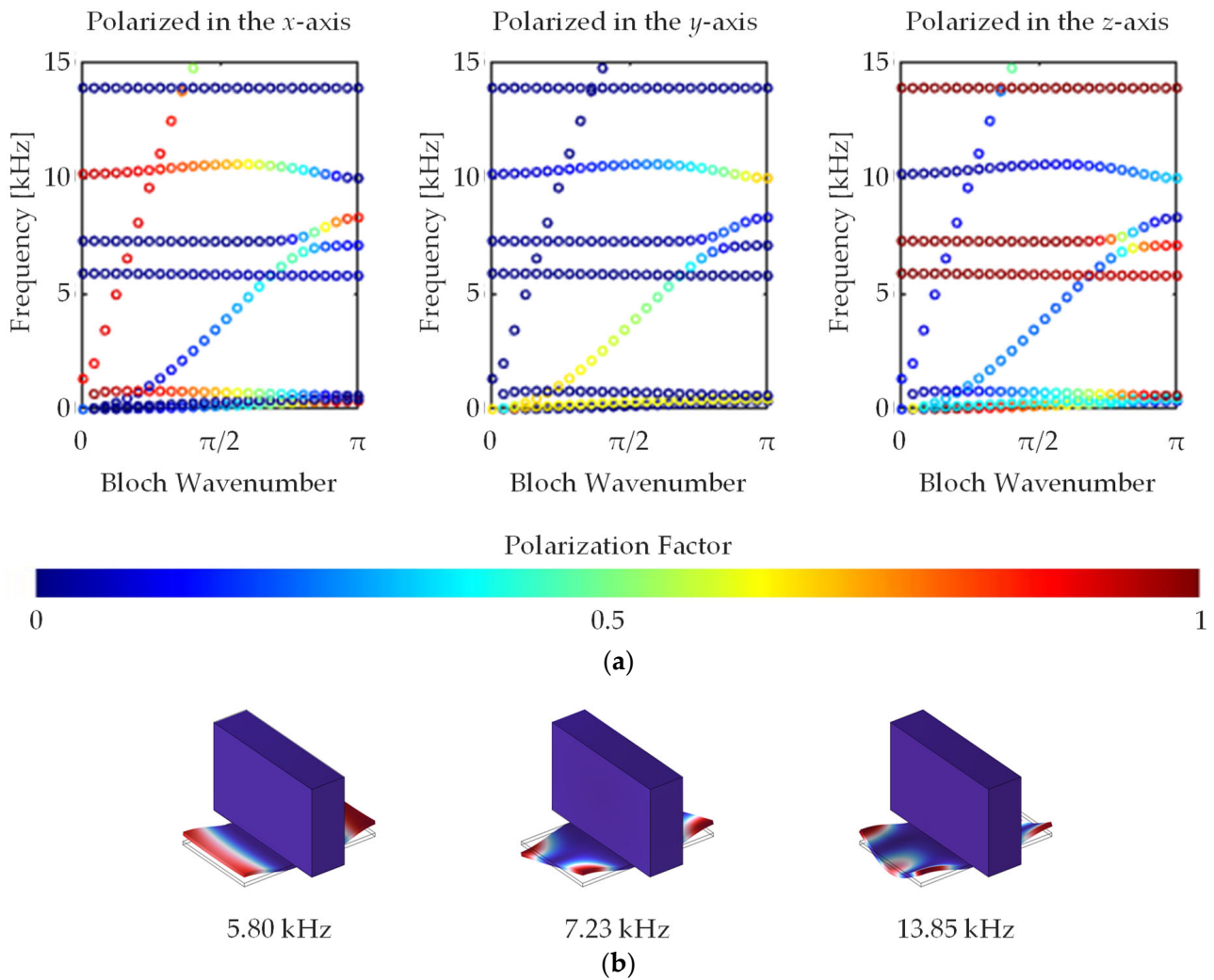


Figure 2. Identification of the phononic band-gap range at the unit-cell level: (a) band-structure results with the information of polarization factors and (b) several resonant mode shapes at the frequencies of 5.80 kHz, 7.23 kHz, and 13.85 kHz.

At this juncture, one might question why the band-gap analysis is limited to frequencies down to 15 kHz. This limitation is due to the performance constraints of the shaker used in the experiments, as will be discussed in the subsequent section. The shaker is capable of producing normal oscillations only up to 14 kHz, beyond which it becomes overloaded. In practical experiments, the focus is on the frequency range of 1 kHz to 12 kHz to ensure the safe operation of the equipment. Consequently, the band-gap analysis is conducted with this instrumental limitation in mind, focusing solely on the starting frequency of the band gap. Therefore, keeping the specification of the shaker in mind, the unit-cell design is properly structured to perform the defect-band analysis.

Figure 3 presents an example of the calculated defect-band frequencies and defect-mode shapes within the frequency range from 1 to 12 kHz for the defect length of 70 mm, tailored to the testbed setting. The defect-mode shapes are referred to as the overall displacement field of defective PnCs (referred to as *solid.disp* in COMSOL). A total of seven defect bands are observed, which are categorized into three types based on their characteristics. Given the thinness of the beam, it can be assumed that there is no change in displacement field along the z-axis within the defect.

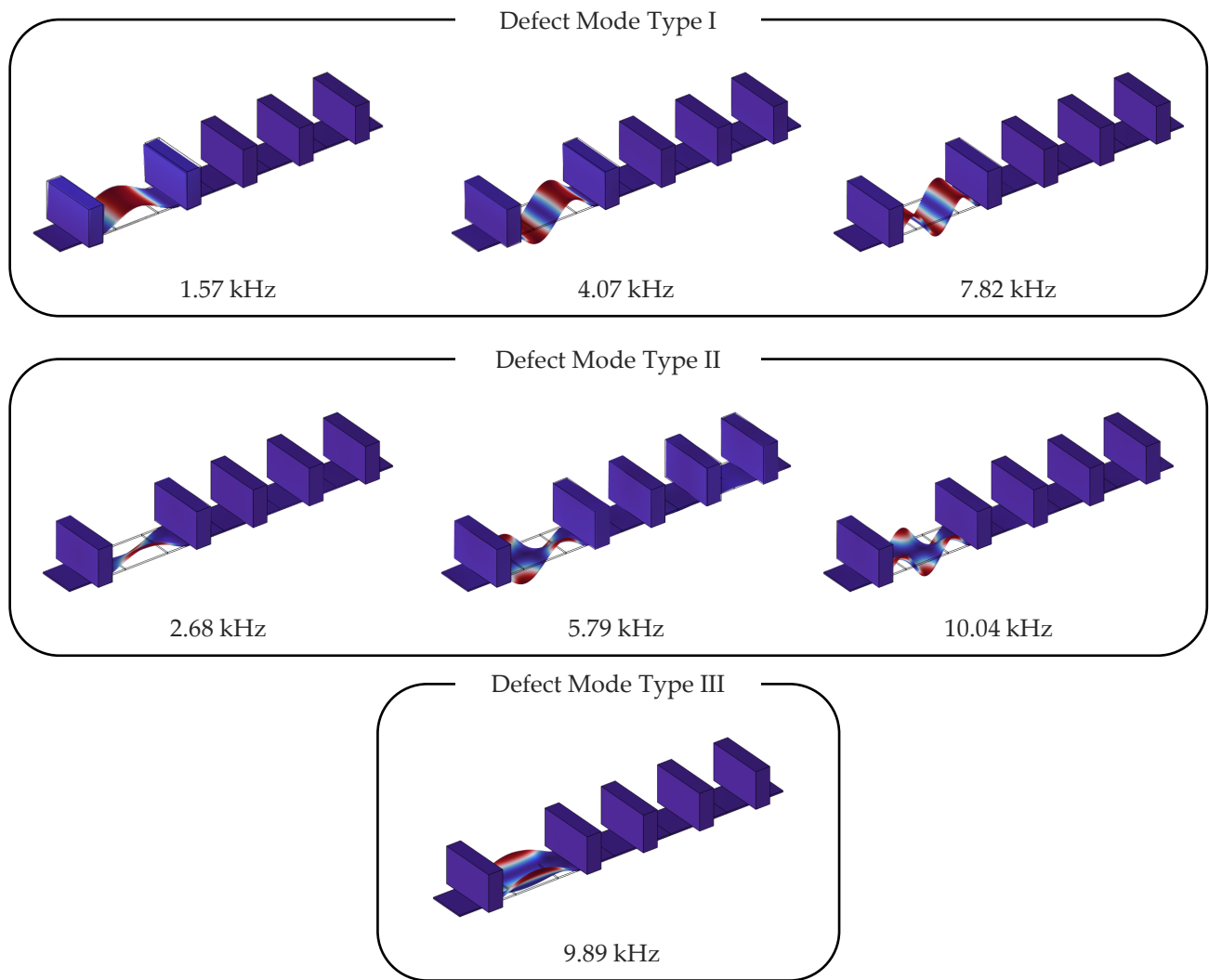


Figure 3. An example of the results from defect-band analysis for a defect length of 70 mm that includes the defect-band frequencies and defect-mode shapes.

Type I are characterized by constant displacement fields along the y -axis, with total displacement within the defect dominated by the x -coordinate. Viewed from the front, the defect-mode shapes in the x -axial direction exhibit a half-period cosine function at 1.57 kHz, a one-period sine function at 4.07 kHz, and a 1.5-period cosine function at 7.82 kHz relative to the center of the defect. Type II has displacement fields that are point-symmetric with respect to the xy -plane, meaning the total displacement fields within the defect are influenced by both x - and y -coordinates. For displacement fields at the edge of the beam, when viewed from the front, the defect-mode shapes in the x -axial direction show a half-period cosine function at 2.68 kHz, a one-period sine function at 5.79 kHz, and a 1.5-period cosine function at 10.04 kHz. Type III exhibits displacement fields that are line-symmetric with respect to the xy -plane. For displacement fields at the edge of the beam, when viewed from the front, the defect modes in the x -axial direction are observed with a half-period cosine function at 9.89 kHz. Type I refers to the energy-localized behaviors observed in typical beams, while Types I and II describe the energy-localized behaviors observed in plates.

In the last paragraph of the previous section, we mentioned that the required minimum length of a lattice constant is 40 mm from the perspective of magnetic forces. Given that the metal beam used in the experiment is 300 mm long, the lattice constant of 40 mm was chosen. At this point, one may wonder how defect-band frequencies change in terms of the

lattice constant. To answer this question, Figure 4 varies the lattice constant from 20 mm to 60 mm in 5 mm increments, while keeping the defect length fixed at 70 mm. The bottom light gray area in the figure represents the region outside the band gap where passbands are observed. The top dark gray area indicates where vibrations cannot be excited by the shaker. Therefore, the results within the white background are of primary interest. The solid lines in red, blue, and green correspond to Types I, II, and III in Figure 3, respectively. There are two key observations to note. First, as the lattice constant increases, the lower edge of the band-gap range decreases. This is a typical phenomenon for band gaps induced by Bragg scattering. Second, the defect bands show little change as the lattice constant is varied. One recent theoretical study demonstrates that evanescent waves, which characterize phononic band gaps, can induce virtual fixed-end boundary conditions in unit cells adjacent to a defect [49]. This induces resonating motion near the defect at each defect-band frequency. In this design, the difference between the mechanical impedances of the defect, corresponding to the thin metal beam, and the thick ferrite magnets on either side is considerably large, causing the adjacent two magnets to directly create the fixed-like boundary condition. For this reason, the defect-band frequencies remain constant regardless of the spacing of the unit cells outside the defect. Furthermore, Figure 3 visually demonstrates that there is almost no mechanical motion in the structures outside of the defect.

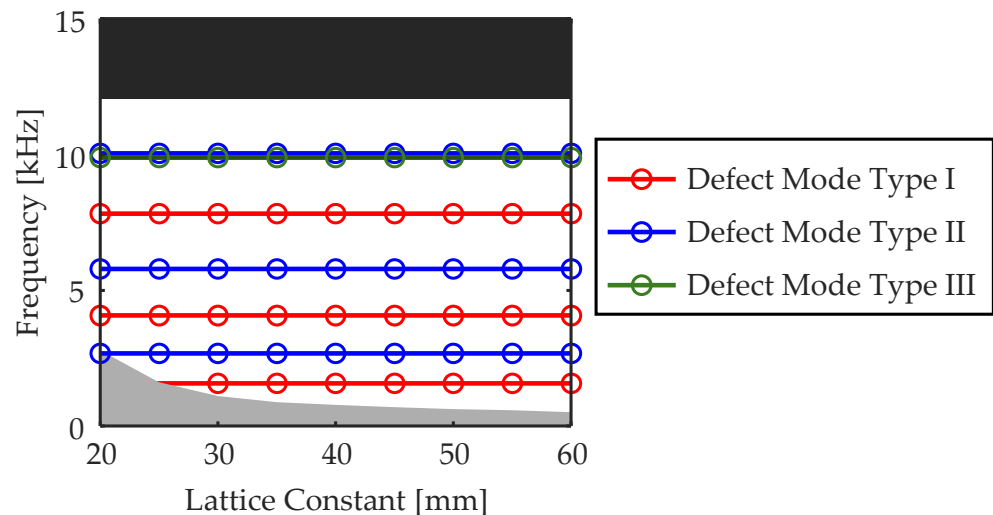


Figure 4. Effects of the lattice constant on defect-band frequencies when the defect length is fixed at 70 mm.

4. Experimental Setup and Procedure

Figure 5a presents a front view of the experimental testbed, which comprises the following equipment and/or components: a function generator (Keysight, EDU33212A, Santa Rosa, CA, USA), a set of a miniature shaker (Brüel and Kjær, Type 4810, Nærum, Denmark) and power amplifier (Brüel and Kjær, Type 2718, Nærum, Denmark), an accelerometer (PCB Piezotronics, 333B40 SN 59572, Depew, NY, USA), a conditioning amplifier (Dytran, 4103C, Chatsworth, CA, USA), an oscilloscope (Keysight, DSOX1204A, Santa Rosa, CA, USA), and a support. Several components are labeled in this figure. Referring to previous studies that validate the effectiveness of PnCs through experiments, this setup is considered typical [50–52].

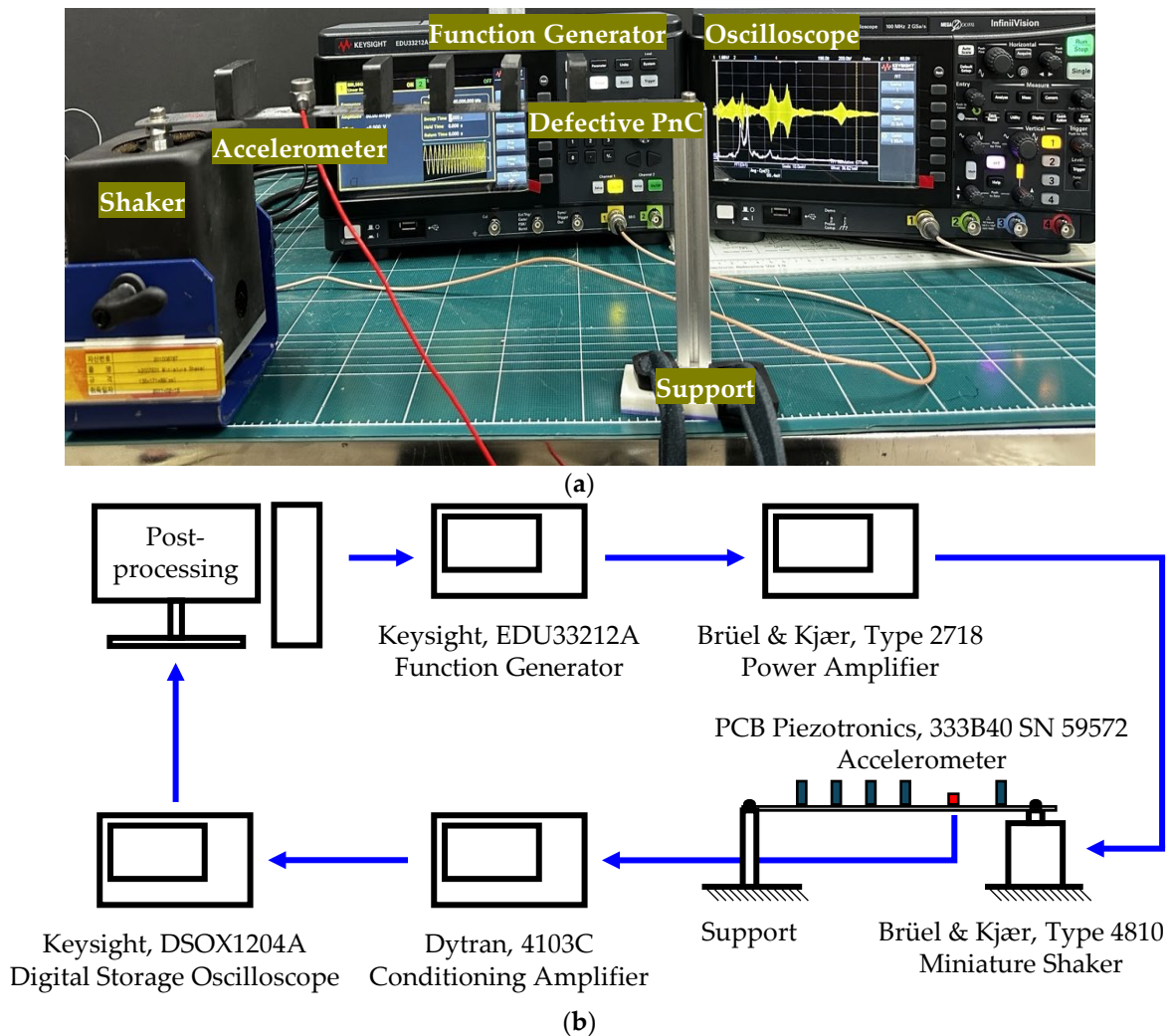


Figure 5. Experimental setup and procedure: (a) several equipment and components to measure the acceleration responses at the center of the defect and (b) a schematic diagram of the experimental setup from inputting excitation signals to saving acceleration responses.

Figure 5b depicts a schematic diagram of the experimental setup. An excitation signal generated by the function generator is input into the miniature shaker using the power amplifier. The top of the shaker is physically connected to the left end of the 300 mm steel beam, ensuring synchronized vertical (bending) movements between the shaker and the steel beam. The right end of the steel beam is secured by the support, maintaining a fixed position. This setup is designed to eliminate unwanted factors caused by the deflection of the steel beam due to the self-weight of the beam and magnets. In low frequencies, the same setup was employed in one previous study where experimental measurements of energy-localization performance were conducted on beam-type elastic metamaterials [53]. Furthermore, it was previously demonstrated through numerical analyses that the generation of defect modes was independent of the boundary condition settings (e.g., free and fixed conditions) of defective PnCs [54]. Subsequently, an accelerometer is bonded to the center of the defect with the help of epoxy to measure vibration signals over time. After amplification and simple signal processing using the conditioning amplifier, the oscilloscope is utilized not only to visualize the measured acceleration but also to store the data.

Figure 6 visualizes the excitation condition employed in the experiment. Specifically, it displays the screen observed by the user when operating the function generator. In this study, the linear sine sweep function is utilized to observe the frequency response

function (FRF) for the acceleration measured at the center of the defect. The linear sine sweep function, with frequency proportional to time, is characterized by Equation (5):

$$v(t) = \sin\left(2\pi\left(f_{\text{start}} t + \frac{f_{\text{stop}} - f_{\text{start}}}{2T} t^2\right)\right) \quad (5)$$

where f_{start} and f_{stop} denote the start frequency and stop frequency, respectively. T represents the sweep time, and t indicates time. v stands for the input voltage. The start frequency f_{start} is set at 1 kHz, and the stop frequency f_{stop} is set at 12 kHz. It is noteworthy that the maximum frequency allowed by the shaker is 14 kHz, rendering this frequency range appropriate. The sweep time is 2 s, with both the hold time and return time set to 0 s. A visual representation of this function is provided in the right corner of Figure 6. Utilizing this sine sweep function, the measured acceleration may encompass frequencies ranging from 1 to 12 kHz over a duration of 2 s. The existing literature has experimentally measured defect-band frequencies and wave-localization performance using sine waves with single frequencies (called monochromatic waves) and passively varying the excitation frequency. However, since this study specifically focuses on the variation in defect-band frequencies, this kind of excitation setting is adopted.

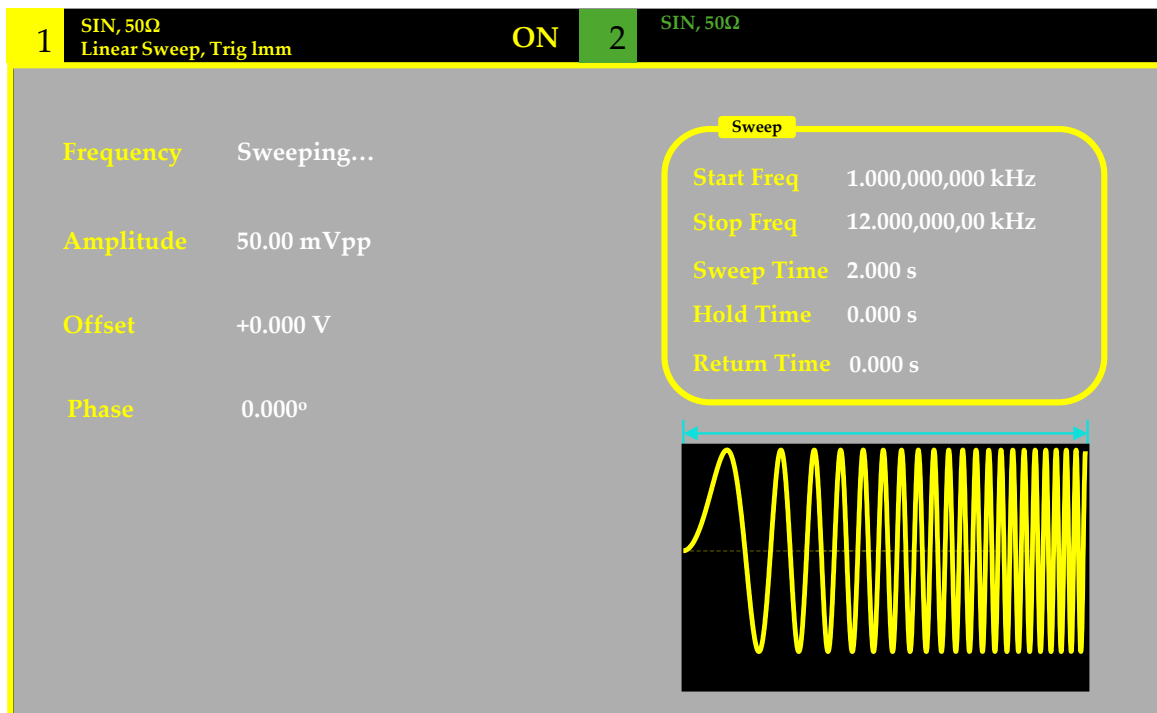


Figure 6. A setting of the linear sine sweep function considered in the function generator.

Note that vibration test equipment and sensors should be calibrated regularly. In this experiment, calibration was performed by a specialized company in the Republic of Korea at the beginning of 2024, ensuring reliable experimental results. It is also necessary to account for measurement errors. For example, is a similar time-series profile consistently obtained under identical vibration conditions? To address this, we conducted 100 repeated measurements for each scenario to confirm that similar data are achieved and saved after applying ensemble techniques. Although there may be differences in the data depending on the method (e.g., point-joint or line-joint) of joining the metal beam and shaker, the consistent joining of the metal beam and shaker yields reproducible results. Indeed, when the magnets were removed and the same experiment for the same defect length was performed on a different day, similar data were repeatedly measured.

5. Experiment Results and Discussion

Before presenting and analyzing the experimental data, it is important to mention a key detail. In Figure 3, seven distinct defect-mode shapes are displayed, but our focus is specifically on Defect Mode Type I. Moreover, within Defect Mode Type I, we only observe the first and third defect-mode shapes. There are two possible explanations for this selective observation. First, since the accelerometer is placed at the center of the defect, the remaining five defect-mode shapes exhibit almost zero displacement at this location. Consequently, even if these modes were present, the acceleration measured at the center of the defect would be difficult to detect. This raises the question: why measure acceleration at the center of the defect? This leads to the second reason. Previous studies have shown that for applications such as energy harvesters and ultrasonic devices (e.g., sensors and actuators), displacement fields with both positive and negative strains reduce output performance due to voltage cancelation within piezoelectric material [55–57]. Consequently, these five defect-mode shapes are excluded from the present experimental results.

Figure 7a illustrates one example of the experimentally measured acceleration signal in a time series when the defect length is approximately 70 mm. The x -axis represents the time domain from 0 to 2 s, while the y -axis indicates the acceleration ranging from -5 V to 5 V. Although the signal appears somewhat complex, it is possible to observe a pattern where the measured value increases at certain time points, decelerates sharply, and then increases again. As previously mentioned, in a linear sine sweep, time is linearly proportional to frequency, implying that the acceleration may be highly amplified or reduced at specific frequency ranges. To confirm this conjecture, a fast Fourier transform (FFT) technique is applied. This function is already stored in the oscilloscope. The acceleration amplitude in the frequency domain is presented in Figure 7b. The x -axis spans the frequency domain from 0 to 12 kHz, and the y -axis displays the normalized acceleration amplitude from 0 to 1. It should be noted that normalization is achieved by dividing the FFT results by their maximum value. As anticipated, this figure reveals peaks in acceleration values at several specific frequencies. The defect-band frequencies of the corresponding defective PnC are highlighted with red circles in Figure 7b. These measurement and post-processing procedures have been used in Ref. [58].

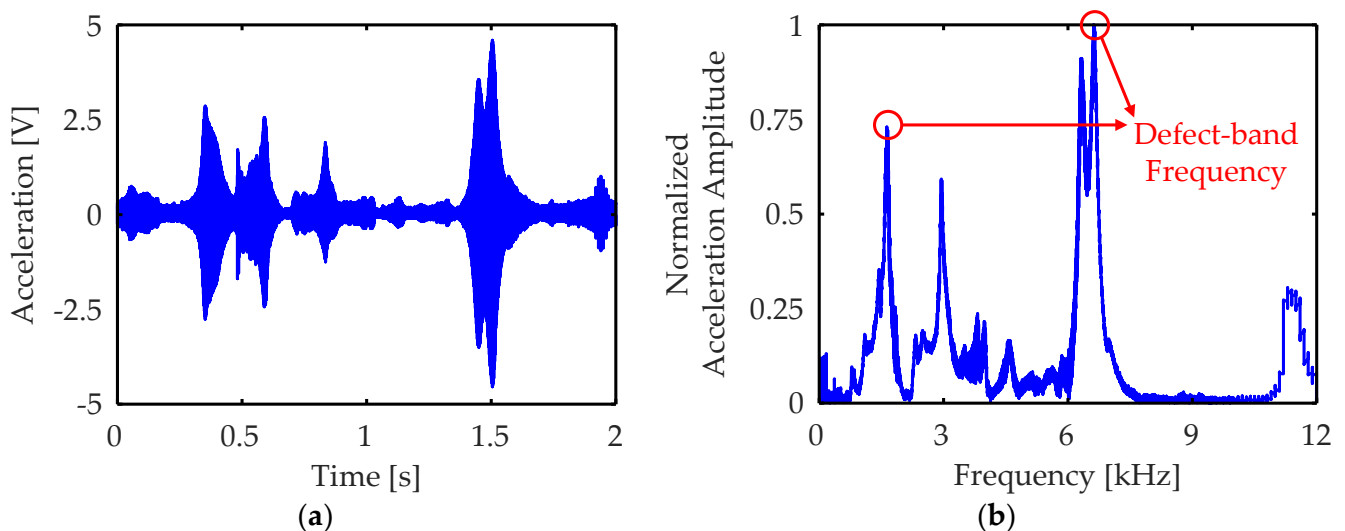


Figure 7. One example of obtaining the information of defect-band frequencies in the experiment; (a) the measured acceleration signal in the time domain and (b) the normalized acceleration amplitude in the frequency domain transformed through FFT techniques.

At this point, one may be wondering why these highlighted frequencies are identified as defect-band frequencies despite observing multiple peaks. There are three possible explanations for this phenomenon. First, the geometric deviation between the steel beam

and the ferrite magnets is significant. Given the substantial mass, volume, and mechanical impedances of the ferrite magnets, they exhibit their own mechanical resonances, as shown in Figure 2b. These motions can contribute to the appearance of resonance-related peaks. Second, due to the finite length of the present PnC structure, multiple reflections inevitably occur at both ends of the steel beam. Furthermore, finite boundary conditions imply that the defective PnC can exhibit various structural resonance frequencies, irrespective of the defect's nature. These effects of reflections and resonant behaviors can bring about additional peaks. Last, uncertainty regarding the accelerometer position may have led to the observation of the five defect-mode shapes in Figure 3 that were not intended for observation. Therefore, a parametric study of defect bands along each defect length is preliminarily conducted, and the appropriate peak frequencies in the vicinity of the target defect-band frequencies are selected.

Figure 8 illustrates the variation in defect-band frequencies as the defect length is mechanically adjusted. The red line represents the numerically calculated results using COMSOL Multiphysics, while the blue line denotes the experimentally measured results. The x -axis represents the defect length, which increases from 50 to 90 mm in 5 mm increments, and the y -axis represents the frequency range from 0 to 12 kHz. A notable observation is that the numerically calculated defect bands are approximately three, while the experimentally measured defect bands are two. This investigation aligns with the statement at the beginning of this section.

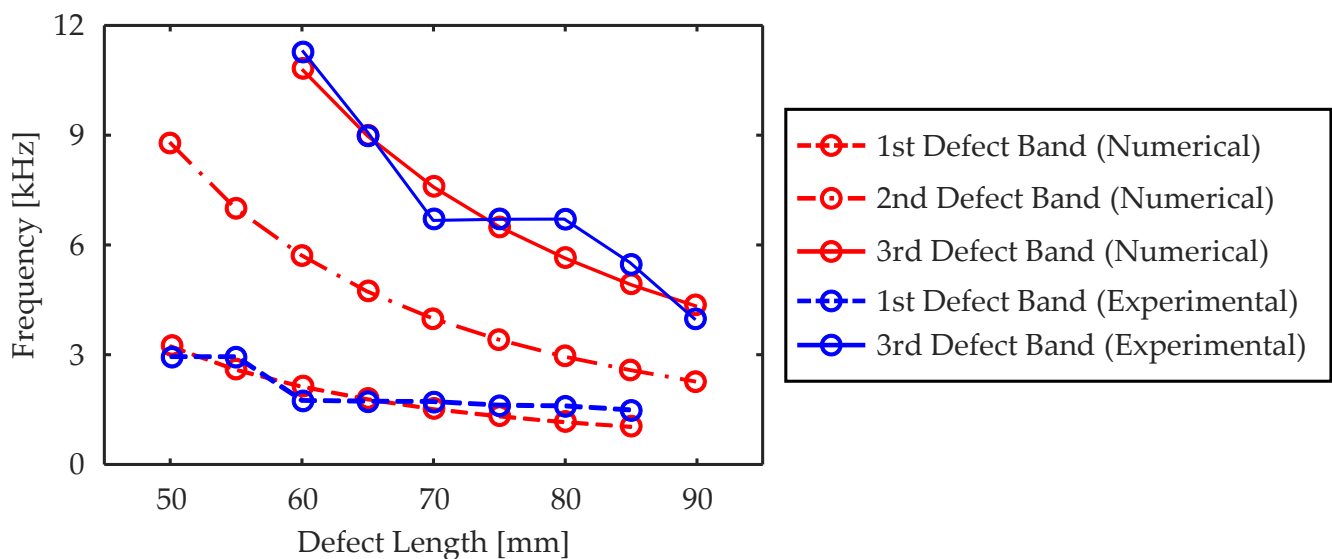


Figure 8. A comparison between the numerical and experimental results of defect-band frequencies across several defect lengths.

Two key observations can be made. First, the numerically predicted and experimentally measured results exhibit similar trends within a comparable range. To analyze this accuracy more quantitatively, we use the coefficient of determination (called R-square) as an evaluation metric. Referring to Figure 3, the R-square value is 0.93 for the low-frequency defect-band corresponding to the first defect-mode shape and 0.84 for the high-frequency defect-band corresponding to the third defect-mode shape. This indicates a good statistical fit between the experimental and numerical results. The primary sources of error can be attributed to physical uncertainties. The material properties used in the analysis are obtained from the data sheets built into COMSOL or provided by the suppliers. As such, they do not represent the true values for the materials used in the present experiment, introducing inaccuracies. Additionally, there is a margin of error in the magnet positions due to manual manipulation. Lastly, during the experiment, it is observed that the connection between the shaker and the metal beam is slightly loosened, which may contribute to small errors. Second, both defect-band frequencies decrease as a fractional function as the defect

length increases. As mentioned in the Introduction, defect-mode-based energy localization is directly related to the mechanical resonance of the defect, and it is well established that the mechanical resonance frequency decreases with increasing structural length. Our experimental findings corroborate this relationship both numerically and experimentally. These considerations collectively suggest that the methodology for designing defective PnCs using permanent magnets and ferromagnetic materials, along with mechanically controlling the defect band, has been successfully validated.

6. Conclusions

In conclusion, this study successfully demonstrated the efficacy of mechanically tunable defect bands in one-dimensional reconfigurable phononic crystals (PnCs) utilizing permanent magnets and ferromagnetic materials. The case study involved attaching five ferrite magnet blocks to a long steel beam through magnetic forces. By altering the relative positioning of selected ferrite magnet blocks, a defect was readily created, enabling the formation and adjustment of defect bands. This method provided a robust mechanism for the mechanical tuning of defect bands. The significant magnetic forces ensured the structural stability of the defective PnC during oscillatory excitation, preventing detachment even when the defective PnC was subjected to gravitational forces. Experimental results, consistent with numerical predictions, confirmed that defect-band frequencies decreased with increasing defect length, corroborating the relationship between mechanical resonance frequency and structural length.

The proposed design significantly enhances the practicality of defective PnCs by eliminating the need for complex geometric alterations or the attachment of elastic foundations, which often complicates the adjustment process. Several future research directions are recommended. First, it is essential to investigate the long-term durability and maintenance requirements of PnCs in harsh environments. Second, in the presence of magnetic materials within the surrounding environment of the targeted systems, mechanisms must be devised to ensure the robust operation of the proposed design, along with techniques for compact embedding. Lastly, further miniaturization of the proposed design is necessary to facilitate its application at much higher frequencies. By pursuing these future research directions, the functionality, efficiency, and practical applicability of reconfigurable defective PnCs can be further enhanced in a wide range of technological domains.

Leveraging the adjustable defect-band properties of reconfigurable defective PnCs offers significant potential for the development of complex mechanical logic circuits, such as demultiplexers and multiplexers. Furthermore, advancements in tunable ultrasonic sensors and transducers can substantially expand the applications of defective PnCs in fields such as medical imaging, prognostics and health management, and structural health monitoring. For instance, in Refs. [28,29], defect modes are employed to amplify frequencies associated with faulty modes of rotating machinery. By further advancing the proposed design concept and embedding it in a compact hardware device, reconfigurable defective PnCs can be utilized to detect various fault signal frequencies in different mechanical systems.

Author Contributions: Conceptualization, S.-H.J.; methodology, J.Y. and S.-H.J.; software, J.Y. and S.-H.J.; validation, J.Y. and S.-H.J.; formal analysis, J.Y. and S.-H.J.; investigation, J.Y. and S.-H.J.; writing—original draft preparation, S.-H.J.; writing—review and editing, S.-H.J.; visualization, J.Y. and S.-H.J.; supervision, S.-H.J.; project administration, S.-H.J.; funding acquisition, S.-H.J. All authors have read and agreed to the published version of the manuscript.

Funding: This work was supported by the Basic Science Research Program through the National Research Foundation of Korea (NRF), funded by the Ministry of Education under Grant 2022R1I1A1A01056406.

Data Availability Statement: Data are contained within the article.

Acknowledgments: The authors would like to express our sincere gratitude to Moon K. Kwak, Dae W. Kim, Junho Yoon, and Soo Min Kim (Dongguk University) for their assistance in renting the experimental equipment and providing a detailed manual.

Conflicts of Interest: The authors declare no conflicts of interest.

References

1. Oudich, M.; Gerard, N.J.; Deng, Y.; Jing, Y. Tailoring structure-borne sound through bandgap engineering in phononic crystals and metamaterials: A comprehensive review. *Adv. Funct. Mater.* **2023**, *33*, 2206309. [[CrossRef](#)]
2. Wang, Y.; Xu, X.; Li, L. Advances in tunable bandgaps of piezoelectric phononic crystals. *Materials* **2023**, *16*, 6285. [[CrossRef](#)]
3. Akbari-Farahani, F.; Ebrahimi-Nejad, S. From defect mode to topological metamaterials: A state-of-the-art review of phononic crystals & acoustic metamaterials for energy harvesting. *Sens. Actuators A Phys.* **2024**, *365*, 114871.
4. Zhao, P.; Yuan, L.; Ma, T.; Wei, H. Study on tunable band gap of flexural vibration in a phononic crystals beam with PBT. *Crystals* **2021**, *11*, 1346. [[CrossRef](#)]
5. Zhang, Z.; Qian, D.; Zou, P. Study on band gap characteristics of phononic crystal double-layer beam structure attached by multilayer cylinder. *Crystals* **2023**, *13*, 638. [[CrossRef](#)]
6. Zhang, G.; Gao, X.; Wang, S.; Hong, J. Bandgap and its defect band analysis of flexoelectric effect in phononic crystal plates. *Eur. J. Mech. A Solids* **2024**, *104*, 105192. [[CrossRef](#)]
7. Cao, D.-X.; Li, S.-S.; Guo, X.-Y.; Chen, X.-M.; Lai, S.-K. Buckling-driven piezoelectric defect-induced energy localization and harvesting using a Rubik's cube-inspired phononic crystal structure. *Smart Mater. Struct.* **2024**, *33*, 035036. [[CrossRef](#)]
8. Kirchhof, J.N.; Weinel, K.; Heeg, S.; Deinhart, V.; Kovalchuk, S.; Höflich, K.; Bolotin, K.I. Tunable graphene phononic crystal. *Nano Lett.* **2021**, *21*, 2174–2182. [[CrossRef](#)]
9. Li, J.; Guo, J.; Zhang, Z. Enhanced energy localization and harvesting by design of phononic crystal defects. *Int. J. Mod. Phys. B* **2024**, *38*, 2450244. [[CrossRef](#)]
10. Jo, S.-H.; Youn, B.D. Designing a phononic crystal with a defect for target frequency matching using an analytical approach. *Mech. Adv. Mater. Struct.* **2022**, *29*, 2454–2467. [[CrossRef](#)]
11. Lee, G.; Park, J.; Choi, W.; Ji, B.; Kim, M.; Rho, J. Multiband elastic wave energy localization for highly amplified piezoelectric energy harvesting using trampoline metamaterials. *Mech. Syst. Signal Process.* **2023**, *200*, 110593. [[CrossRef](#)]
12. Shu, Z.; Zhang, G.; Cong, Y.; Gu, S. Size effects on a one-dimensional defective phononic crystal sensor. *Smart Mater. Struct.* **2023**, *32*, 115029. [[CrossRef](#)]
13. Jo, S.-H.; Lee, D. An improved analytical model of a thick defective phononic crystal for bending wave excitation. *Int. J. Mech. Sci.* **2024**, *264*, 108822. [[CrossRef](#)]
14. Jo, S.-H.; Youn, B.D. An improved analytical model that considers lateral effects of a phononic crystal with a piezoelectric defect for elastic wave energy harvesting. *Int. J. Mech. Sci.* **2021**, *205*, 106593. [[CrossRef](#)]
15. He, Z.; Zhang, G.; Chen, X.; Cong, Y.; Gu, S.; Hong, J. Elastic wave harvesting in piezoelectric-defect-introduced phononic crystal microplates. *Int. J. Mech. Sci.* **2023**, *239*, 107892. [[CrossRef](#)]
16. Hosseinkhani, A.; Ebrahimi, F.; Younesian, D.; Moayedizadeh, A. Defected meta-lattice structures for the enhanced localized vibrational energy harvesting. *Nano Energy* **2022**, *100*, 107488. [[CrossRef](#)]
17. Jo, S.-H.; Youn, B.D. An explicit solution for the design of a target-frequency-customized, piezoelectric-defect-introduced phononic crystal for elastic wave energy harvesting. *J. Appl. Phys.* **2021**, *130*, 184902. [[CrossRef](#)]
18. Wang, K.; Li, X.-S.; Cao, L.; Guo, P.; Fan, G.; Qin, J.; Ma, T.-X. Enhancement of piezoelectric energy harvesting for flexural waves by a metasurface-assisted phononic cavity. *Results Phys.* **2024**, *63*, 107870. [[CrossRef](#)]
19. Zhang, X.; Li, Y.; Wang, Y.; Jia, Z.; Luo, Y. Narrow-band filter design of phononic crystals with periodic point defects via topology optimization. *Int. J. Mech. Sci.* **2021**, *212*, 106829. [[CrossRef](#)]
20. Zhong, J.; Xiang, J. Designing a phononic crystal with a large defect to enhance elastic wave energy localization and harvesting. *Jpn. J. Appl. Phys.* **2022**, *61*, 017002.
21. He, J.; Sun, J.; Fan, J.; Jia, Z.; Zhang, X. Optimal designs of phononic crystal microstructures considering point and line defects. *Symmetry* **2021**, *13*, 1993. [[CrossRef](#)]
22. Lee, D.; Youn, B.D.; Jo, S.-H. Deep-learning-based framework for inverse design of a defective phononic crystal for narrowband filtering. *Int. J. Mech. Sci.* **2023**, *255*, 108474. [[CrossRef](#)]
23. Lv, X.-F.; Fang, X.; Zhang, Z.-Q.; Huang, Z.-L.; Chuang, K.-C. Highly localized and efficient energy harvesting in a phononic crystal beam: Defect placement and experimental validation. *Crystals* **2019**, *9*, 391. [[CrossRef](#)]
24. Wang, X.; Jiang, P.; Chen, T.; Yu, K. Frequency characteristics of defect states in a two-dimensional phononic crystal with slit structure. *Int. J. Mod. Phys. B* **2016**, *30*, 1650025. [[CrossRef](#)]
25. Alrowaili, Z.; Fathy, H.M.; Elsayed, H.A.; Aouassa, M.; Mahmoud, M.; El-Nasser, K.S.; Taha, T.; Mehaney, A. Heavy metals biosensor based on defective one-dimensional phononic crystals. *Ultrasonics* **2023**, *130*, 106928. [[CrossRef](#)] [[PubMed](#)]
26. Geng, Q.; Cai, T.; Li, Y. Flexural wave manipulation and energy harvesting characteristics of a defect phononic crystal beam with thermal effects. *J. Appl. Phys.* **2019**, *125*, 035103. [[CrossRef](#)]
27. Gantasala, S.; Thomas, T.; Rajagopal, P. Enhanced piezoelectric energy harvesting based on sandwiched phononic crystal with embedded spheres. *Phys. Scr.* **2023**, *98*, 035029. [[CrossRef](#)]
28. Xiao, J.; Ding, X.; Wang, Y.; Huang, W.; He, Q.; Shao, Y. Gear fault detection via directional enhancement of phononic crystal resonators. *Int. J. Mech. Sci.* **2024**, *278*, 109453. [[CrossRef](#)]

29. Xiao, J.; Ding, X.; Huang, W.; He, Q.; Shao, Y. Rotating machinery weak fault features enhancement via line-defect phononic crystal sensing. *Mech. Syst. Signal Process.* **2024**, *220*, 111657. [[CrossRef](#)]
30. Yoo, J.; Park, J.; Kim, T.; Ha, J.M.; Youn, B.D. Weighted multi-order Viterbi algorithm (WMOVA): Instantaneous angular speed estimation under harsh conditions. *Mech. Syst. Signal Process.* **2024**, *211*, 111187. [[CrossRef](#)]
31. Lee, S.K.; Kim, H.; Chae, M.; Oh, H.J.; Yoon, H.; Youn, B.D. Self-supervised feature learning for motor fault diagnosis under various torque conditions. *Knowl. Based Syst.* **2024**, *288*, 111465. [[CrossRef](#)]
32. Lee, S.; Kim, S.; Kim, S.J.; Lee, J.; Yoon, H.; Youn, B.D. Revolution and peak discrepancy-based domain alignment method for bearing fault diagnosis under very low-speed conditions. *Expert Syst. Appl.* **2024**, *251*, 124084. [[CrossRef](#)]
33. Yao, B.; Wang, S.; Hong, J.; Gu, S. Size and temperature effects on band gap analysis of a defective phononic crystal beam. *Crystals* **2024**, *14*, 163. [[CrossRef](#)]
34. Geng, Q.; Fong, P.-K.; Ning, J.; Shao, Z.; Li, Y. Thermally-induced transitions of multi-frequency defect wave localization and energy harvesting of phononic crystal plate. *Int. J. Mech. Sci.* **2022**, *222*, 107253. [[CrossRef](#)]
35. Geng, Q.; Wang, T.; Wu, L.; Li, Y. Defect coupling behavior and flexural wave energy harvesting of phononic crystal beams with double defects in thermal environments. *J. Phys. D Appl. Phys.* **2021**, *54*, 225501. [[CrossRef](#)]
36. Jo, S.-H. Electrically controllable behaviors in defective phononic crystals with inductive-resistive circuits. *Int. J. Mech. Sci.* **2024**, *278*, 109485. [[CrossRef](#)]
37. Jo, S.-H.; Park, M.; Kim, M.; Yang, J. Tunable bandpass filters using a defective phononic crystal shunted to synthetic negative capacitance for longitudinal waves. *J. Appl. Phys.* **2024**, *135*, 164502. [[CrossRef](#)]
38. Wu, L.-Y.; Wu, M.-L.; Chen, L.-W. The narrow pass band filter of tunable 1D phononic crystals with a dielectric elastomer layer. *Smart Mater. Struct.* **2008**, *18*, 015011. [[CrossRef](#)]
39. Gu, C.; Jin, F. Research on the tunability of point defect modes in a two-dimensional magneto-elastic phononic crystal. *J. Phys. D Appl. Phys.* **2016**, *49*, 175103. [[CrossRef](#)]
40. Li, Y.; Chen, T.; Wang, X.; Ma, T.; Jiang, P. Acoustic confinement and waveguiding in two-dimensional phononic crystals with material defect states. *J. Appl. Phys.* **2014**, *116*, 024904. [[CrossRef](#)]
41. Ma, T.-X.; Fan, Q.-S.; Zhang, C.; Wang, Y.-S. Acoustic flatbands in phononic crystal defect lattices. *J. Appl. Phys.* **2021**, *129*, 145104. [[CrossRef](#)]
42. Jiang, P.; Wang, X.-P.; Chen, T.-N.; Zhu, J. Band gap and defect state engineering in a multi-stub phononic crystal plate. *J. Appl. Phys.* **2015**, *117*, 154301. [[CrossRef](#)]
43. Zhang, G.; He, Z.; Wang, S.; Hong, J.; Cong, Y.; Gu, S. Elastic foundation-introduced defective phononic crystals for tunable energy harvesting. *Mech. Mater.* **2024**, *191*, 104909. [[CrossRef](#)]
44. Shen, W.; Cong, Y.; Gu, S.; Yin, H.; Zhang, G. A generalized supercell model of defect-introduced phononic crystal microplates. *Acta Mech.* **2024**, *235*, 1345–1360. [[CrossRef](#)]
45. Ding, T.; Song, A.; Sun, C.; Xiang, Y.; Xuan, F.-Z. Mode conversion of Lamb waves in a composite phononic crystal plate: Numerical analysis and experimental validation. *J. Appl. Phys.* **2022**, *132*, 225103. [[CrossRef](#)]
46. Carrillo-Munoz, M.; Sharma, B. Identifying elastic wave polarization and bandgaps in periodic solid media. *Int. J. Mech. Sci.* **2023**, *252*, 108363. [[CrossRef](#)]
47. Friis, L.; Ohlrich, M. Coupling of flexural and longitudinal wave motion in a periodic structure with asymmetrically arranged transverse beams. *J. Acoust. Soc. Am.* **2005**, *118*, 3010–3020. [[CrossRef](#)]
48. Yin, C.; Xiao, Y.; Zhu, D.; Wang, J.; Qin, Q.-H. Design of low-frequency 1D phononic crystals harnessing compression–twist coupling effect with large deflection angle. *Thin-Walled Struct.* **2022**, *179*, 109600. [[CrossRef](#)]
49. Jo, S.-H.; Yoon, H.; Shin, Y.C.; Youn, B.D. Revealing defect-mode-enabled energy localization mechanisms of a one-dimensional phononic crystal. *Int. J. Mech. Sci.* **2022**, *215*, 106950. [[CrossRef](#)]
50. Park, H.W.; Seung, H.M.; Kim, M.; Choi, W.; Oh, J.H. Continuum flexural metamaterial for broadband low-frequency band gap. *Phys. Rev. Appl.* **2021**, *15*, 024008. [[CrossRef](#)]
51. Xia, Y.; Ruzzene, M.; Erturk, A. Bistable attachments for wideband nonlinear vibration attenuation in a metamaterial beam. *Nonlinear Dyn.* **2020**, *102*, 1285–1296. [[CrossRef](#)]
52. Panahi, E.; Hosseinkhani, A.; Khansanami, M.F.; Younesian, D.; Ranjbar, M. Novel cross shape phononic crystals with broadband vibration wave attenuation characteristic: Design, modeling and testing. *Thin-Walled Struct.* **2021**, *163*, 107665. [[CrossRef](#)]
53. Park, H.W.; Seung, H.M.; Choi, W.; Kim, M.; Oh, J.H. Highly tunable low frequency metamaterial cavity for vibration localization. *Sci. Rep.* **2022**, *12*, 9714. [[CrossRef](#)] [[PubMed](#)]
54. Jo, S.-H.; Youn, B.D. Enhanced ultrasonic wave generation using energy-localized behaviors of phononic crystals. *Int. J. Mech. Sci.* **2022**, *228*, 107483. [[CrossRef](#)]
55. Erturk, A.; Tarazaga, P.A.; Farmer, J.R.; Inman, D.J. Effect of strain nodes and electrode configuration on piezoelectric energy harvesting from cantilevered beams. *J. Vib. Acoust.* **2009**, *131*, 011010. [[CrossRef](#)]
56. Kim, D.-S.; Choi, W.; Kim, S.-W.; Kim, E.-J.; Nahm, S.; Kim, M. Correlating multimode strain and electrode configurations for high-performance gradient-index phononic crystal-based piezoelectric energy harvesting. *Mater. Horiz.* **2023**, *10*, 149–159. [[CrossRef](#)] [[PubMed](#)]

57. Jo, S.-H.; Youn, B.D. A phononic crystal with differently configured double defects for broadband elastic wave energy localization and harvesting. *Crystals* **2021**, *11*, 643. [[CrossRef](#)]
58. Jo, S.-H.; Shin, Y.C.; Choi, W.; Yoon, H.; Youn, B.D.; Kim, M. Double defects-induced elastic wave coupling and energy localization in a phononic crystal. *Nano Converg.* **2021**, *8*, 27. [[CrossRef](#)]

Disclaimer/Publisher's Note: The statements, opinions and data contained in all publications are solely those of the individual author(s) and contributor(s) and not of MDPI and/or the editor(s). MDPI and/or the editor(s) disclaim responsibility for any injury to people or property resulting from any ideas, methods, instructions or products referred to in the content.